Energy & Environmental Science

Quantification of heterogeneous, irreversible lithium plating in extreme fast charging of Li-ion batteries

Journal:	*Energy & Environmental Science*
Manuscript ID	EE-ART-04-2021-001216.R1
Article Type:	Paper
Date Submitted by the Author:	01-Jul-2021
Complete List of Authors:	Paul, Partha; SLAC National Accelerator Laboratory, Materials Science Thampy, Vivek; SLAC National Accelerator Laboratory Cao, Chuntian; SLAC National Accelerator Laboratory, Stanford Synchrotron Radiation Lightsource; University of Colorado at Boulder Steinrueck, Hans-Georg; SLAC National Accelerator Laboratory, Stanford Synchrotron Radiation Lightsource Tanim, Tanvir; Idaho National Laboratory Dunlop, Alison; Argonne National Laboratory, Chemical Sciences and Engineering Division Dufek, Eric; Idaho National Laboratory, Energy Storage and Advanced Vehicles Trask, Stephen; Argonne National Laboratory, Chemical Sciences and Engineering - Electrochemical Energy Storage Jansen, Andrew; Argonne National Laboratory, Chemical Sciences and Engineering Division Toney, Michael; University of Colorado at Boulder, Nelson Weker, Johanna; SLAC National Accelerator Laboratory,

Energy and Environmental Science

PAPER

Quantification of heterogeneous, irreversible lithium plating in extreme fast charging of Li-ion batteries

Partha P. Paul[a], Vivek Thampy[a], Chuntian Cao[a, b], Hans-Georg Steinrück[a, c], Tanvir R. Tanim[d], Alison R. Dunlop[e], Eric J. Dufek[d], Stephen E. Trask[e], Andrew N. Jansen[e], Michael F. Toney[a, b*], Johanna Nelson Weker[a*]

Realization of extreme fast charging (XFC, ≤15 minutes) of lithium-ion batteries is imperative for the widespread adoption of electric vehicles. However, dramatic capacity fading is associated with XFC, limiting its implementation. To quantitatively elucidate the effects of irreversible lithium plating and other degradation mechanisms on the cell capacity, it is important to understand the links between lithium plating and cell degradation at both the local and global (over the full cell) scales. Here, we study the nature of local lithium plating after hundreds of XFC cycles (charging C-rates ranging from 4C to 9C) in industrially-relevant pouch cells using spatially resolved X-ray diffraction. Our results reveal a spatial correlation at the mm scale between irreversible lithium plating on the anode, inactive lithiated graphite phases, and local state-of-charge of the cathode. In regions of plated lithium, additional lithium is locally and irreversibly trapped as lithiated graphite, contributing to the loss of lithium inventory (LLI) and to a local loss of active anode material. The total LLI in the cell from irreversibly plated lithium is linearly correlated to the capacity loss in the batteries after XFC cycling, with a non-zero offset originating from other parasitic side reactions. Finally, at the global (cell) scale, LLI drives the capacity fade, rather than electrode degradation. We anticipate that the understanding of lithium plating and other degradation mechanisms during XFC gained in this work will help lead to new approaches towards designing high-rate batteries in which irreversible lithium plating is minimized.

Received 00th January 20xx,
Accepted 00th January 20xx

DOI: 10.1039/x0xx00000x

Broader context

Electric vehicles (EVs), powered by lithium-ion batteries (LIBs), have gained increasing prominence as a replacement for gasoline-powered vehicles. Several challenges exist in current LIBs, and addressing them is paramount to the wider adoption of EVs. One prominent challenge is reducing the amount of time needed to recharge EVs, to make this comparable to traditional refueling times. To underscore this challenge, the US Department of Energy has outlined a target of achieving a recharging time of less than 15 minutes, referred to as extreme fast charging (XFC), which would be a three-fold improvement on the fastest commercial superchargers available currently. However, XFC of LIBs is hindered by a dramatic loss of cell capacity over cycling, as well as safety concerns arising from electrical shorts between electrodes. Both of these problems are linked to parasitic lithium plating on the anode caused by locally high overpotentials. A comprehensive understanding of how lithium plating affects the battery performance is of paramount importance. Given the multiscale nature of lithium plating, developing such an understanding will involve unraveling the effect of local lithium plating on the local cathode and anode degradation, as well as its effect on the global battery performance. Distinguishing the local and global effects of lithium plating is achieved in-situ using spatially resolved, high-energy X-ray diffraction. This knowledge will aid in the design of the next generation of high rate LIBs that are resistant to parasitic lithium plating resulting in safer batteries with better performance.

[a] SLAC National Accelerator Laboratory, 2575 Sand Hill Road, Menlo Park, CA. 94025, USA.
[b] Department of Chemical and Biological Engineering, University of Colorado, Boulder, CO 80309, USA.
[c] Department Chemie, Universität Paderborn, Warburger Str. 100, 33098 Paderborn, Germany.
[d] Idaho National Laboratory, 2525 N. Fremont, Idaho Falls, ID 83415, USA.
[e] Argonne National Laboratory, 9700 South Cass Avenue, Lemont, IL 60439, USA.
* Corresponding authors: jlnelson@slac.stanford.edu; Michael.Toney@colorado.edu
†Electronic supplementary Information available: See DOI: 10.1039/x0xx00000x

1 Introduction

There is an ever-increasing demand for electric vehicles (EVs) to replace gasoline-powered vehicles. Currently, one of the major disadvantages of EVs is the long recharging time of lithium-ion batteries (LIBs), typically several hours, compared to the 5-10–minute refueling time in gasoline-powered

vehicles.[1] Therefore, to promote the wider adoption of EVs, the US Department of Energy has stated extreme fast charging (XFC) for LIBs as an immediate target with the specific goal of realizing a recharging time of 15 minutes or less to 80% of full capacity.[2]

However, fast charging of LIBs is associated with several problems, with the most prominent being the rapid loss of battery capacity over cycling.[3; 4; 5] High current densities cause a large potential drop across the thickness of the anode and a large concentration gradient of Li^+,[6; 7] leading to Li metal plating as well as other side reactions at the anode and cathode driven by locally high overpotentials. While some of the plated lithium can be reversibly stripped,[8] the rest either reacts with the electrolyte [5] or loses electrical contact becoming "dead Li".[9; 10] The portion of lithium metal that is not reversibly stripped contributes to the capacity fade through the loss of lithium inventory (LLI).[11; 12] Moreover, the high power densities during XFC can increase the cells' internal temperature, resulting in the increased growth of the solid electrolyte interphase (SEI),[6] which consumes lithium and further reduces the inventory of active lithium. Additionally, the high rates can cause electrode particles to crack and possibly lose electrical contact,[3] resulting in capacity fade through the loss of active electrode materials (LAM). Therefore, to develop rational approaches to mitigate the capacity fading in XFC batteries, it is critical to quantify the capacity loss caused by these different degradation mechanisms[13].

The mechanisms leading to XFC capacity loss can be broadly categorized into LAM and LLI. Tornheim and O'Hanlon differentiate LLI and LAM dominated loss as *'inventory limited'* and *'site limited'* cells respectively.[12] However, the quantitative importance of these loss mechanisms to the capacity fade has not been explored in detail because experimentally *quantifying* the individual contributions of anode and cathode loss to LAM, as well as the contribution of individual mechanisms within LLI (increased solid electrolyte interface (SEI) formation, dead lithium, and others) has proven challenging[14]. For example, optical images prove the presence of plated lithium metal on disassembled cells, but cannot quantify how much lithium metal is present.[15] Post-mortem quantifications of the global cell performance are valuable to correlate cell degradation to the LLI in the cell, but are often limited in quantifying the relative importance of individual loss mechanisms within LLI [16; 17; 18; 19] or the contribution of LAM to cell degradation. In a recent paper, we used high-energy X-ray diffraction (XRD) along with global electrochemical measurements to investigate the capacity fade in LIBs at XFC rates ranging from 1C to 9C, demonstrating that lithium plating was not directly correlated to the C-rate.[20] In a previous study on silicon thin-film electrodes, we combined *operando* X-ray reflectivity with precision electrochemistry measurements to quantify the capacity loss from SEI growth during each cycle,[21] which allowed an assessment of the contribution of SEI to capacity lost over several cycles. Adopting a similar quantitative assessment of the individual parasitic loss mechanisms in XFC on full cells is essential to develop approaches to mitigate increased capacity fading during XFC.

Another obstacle in achieving XFC is the heterogeneous nature of lithium plating, which may aggravate the existing safety issues and affect the degradation of other cell components. Lithium plating creates safety concerns because dendrite growth can short the electrodes,[22] potentially resulting in catastrophic failure of the cell. With the heterogeneity in lithium plating, some locations in the cell are more favorable for lithium plating, which in turn are more vulnerable to lithium dendrite growth and battery shorting. Several hypotheses have been suggested for why lithium plates preferentially in certain cell locations, such as electrolyte wetting inhomogeneity[23] and lithiation concentration gradients across the thickness of the anode or electrolyte.[8; 24] Additionally, this heterogeneity may affect the electrochemical reactions of anode and cathode materials, thus negatively impacting the cell performance.

Lithium plating is known to be spatially heterogeneous both across the surface (laterally) and through the thickness (transverse) of the anode. In the lateral direction, the heterogeneity of lithium plating exists at both the macroscale (mm or sub-mm) and the microscale (from nm to µm). Post-mortem optical images[3; 15] of disassembled cells after XFC cycling show the lateral sub-mm scale heterogeneity. At the microscale, the size of plated lithium crystallites provided information on how different electrolytes[25] and different C-rates[26] affect the local nature of lithium plating. To assess the non-uniformity across the thickness of the anode, depth-profiling X-ray scattering-based studies[8; 27] have shown that lithium plating occurs on the separator side of the anode, which is also seen with optical images. Finegan et al. have also demonstrated that the plated lithium reacts with the graphite underneath, affecting the concentration gradient of lithiated graphite in the discharged state after XFC cycling.[8] Although it is known that lithium plates heterogeneously laterally and vertically, investigations on its role in battery degradation during XFC cycling are limited,[22] as are the relationship between lithium plating and the state-of-charge (SOC) of the anode (LiC_x stages) and cathode. Understanding the effects of heterogeneous lithium plating on battery

degradation is paramount to developing methods to mitigate it and enable XFC technologies.

In this work, we address two major questions about LIB degradation under XFC conditions. *First, what are the global (cell-scale) quantitative LLI and LAM loss processes due to XFC over hundreds of cycles? Second, what are the causes of mm-scale anode and cathode heterogeneity and how does the local lithium plating reflect this local heterogeneity?* Combining spatially resolved in-situ high-energy X-ray diffraction with global electrochemical analyses allows us to achieve both objectives. Standard controlled electrochemical tests quantify the global capacity fade, and XRD examines the structure of all crystalline components of the cell (lithium metal, LiC_x, and cathode). This approach allows us to detect plated lithium and the corresponding local SOCs of the electrodes without requiring a teardown of the cell. In this work, we used mm resolution XRD to directly connect the local lithium plating to the local anode and cathode SOC. Additionally, XRD enables us to quantify the phases present and thus the loss processes in the cell. By rastering across the cell with the X-ray beam, we collect phase concentrations and SOC maps across the full 3.1 x 4.5 cm^2 cell. Such an understanding is essential to design and optimize the next generation of plating-resistant LIBs, which are safe and with consistent XFC capabibilty.

2 Experimental

2.1 Cell Fabrication and Cycling

The cells were assembled as single-layer pouch cells. The cathode consists of a 20-µm thick Al foil current collector and a calendered 71-µm thick NMC532 ($LiNi_{0.5}Mn_{0.3}Co_{0.2}O_2$) electrode with 35.4% nominal porosity. The anode consists of a 10-µm thick Cu current collector and a calendered graphite electrode with a thickness of 70 µm and a nominal porosity of 34.5%. The anode and cathode have loadings of 3 mAh/cm^2 and 2.67 mAh/cm^2, respectively. The electrolyte is 3:7 EC (ethylene carbonate): EMC (ethyl methyl carbonate) by wt %, with 1.2M $LiPF_6$ in a Celgard 2320 separator. These components were vacuum-sealed together in a pouch (polyamide polymer with an aluminum laminated film and a polypropylene-based sealant layer). The nominal active areas of the cathode and anode are ~14.1 cm^2 (approx. 3.1 cm x 4.5 cm) and 14.9 cm^2 respectively. The anode overhang is to minimize edge effects. After assembly, the cells were tap charged to 1.5 V (constant voltage) for 15 minutes to prevent corrosion of the copper current collector by the uncharged graphite, and then rested at open-circuit for 12 hours to allow for electrolyte wetting. Subsequently, the cells underwent formation cycling. The formation cycles consisted of three cycles at C/10 charging and discharging (between 3.0 to 4.1 V at a constant current of 0.21 mA/cm^2), followed by three cycles at C/2 charging and discharging (between 3.0 to 4.1 V at a constant current density of 1.13 mA/cm^2). The cells showed a **12-18%** drop in capacity in the first formation cycle (see *ESI*, Table S1).

After formation cycles, the cells were XFC cycled at a temperature of 30 ± 1 °C and a pressure of ~15-30 kPa[20]. Details on the monitoring of the temperature during XFC are included in the *ESI* (Section A). Different C-rates for charging (ranging from 4C to 9C) were employed, as outlined in Fig. 1. While cells were charged at high C-rates, the discharge was done slowly at C/2 (30 minutes), with a rest period of 15 minutes after the charging and after the discharging steps. The fast charge and slow discharge cycles were chosen to mimic the standard operation of electric vehicles. The voltage window for cycling was 3.0 to 4.1 V. A slow reference performance test (RPT) cycle was done every 25 cycles at C/20 to track the cell capacity with cycling. The RPT cycles were conducted to allow for any reversibly plated lithium to strip from the anode during the slow discharge step. The rationale behind the choice of charging protocols, experimental conditions during cycling and cell assembly are described in detail elsewhere [28].

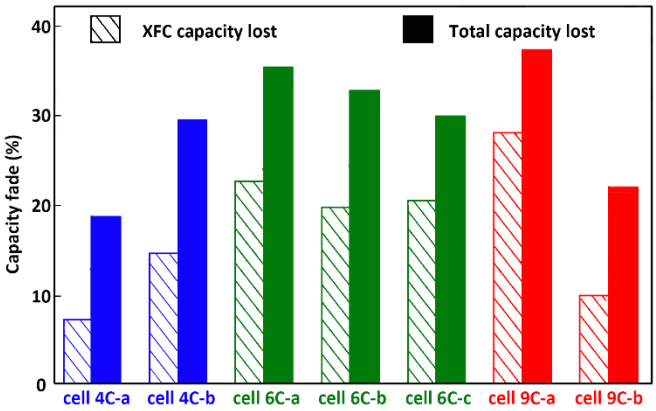

Fig. 1 Performance details of the investigated single-layer pouch cells with graphite anode and NMC ($LiNi_{0.5}Mn_{0.3}Co_{0.2}O_2$) cathode. All cells were subject to six formation cycles, followed by 450 cycles at a charging C-rate as indicated by the cell name (**cell XC** = X C-rate) and with a discharge rate of C/2. The vertical axis shows the capacity lost by each cell during XFC cycling (shaded) and the total capacity lost over formation + XFC cycling (solid color).

2.2 X-ray Diffraction (XRD)

After the 450 XFC cycles, the cells were shipped to Brookhaven National Laboratory at 3.0 V (fully discharged state) for XRD characterization at the National Synchrotron Light Source (NSLS II), Beamline 28-ID-2 in their fully assembled condition. After

characterization of half of the cells at NSLS II, the cells were shipped as is to Argonne National Laboratory to complete the XRD-based characterizations at Advanced Photon Source (APS) beamline 11-ID-B. XRD mapping at NSLS-II Beamline 28-ID-2 was performed with monochromatic 67 keV energy X-rays and at beamline 11-ID-B at APS with 58.6 keV X-rays. The spot size of the X-ray beam on the cells was 0.5 mm x 0.5 mm. The area detector used to collect diffraction patterns was placed at a distance of ~1.3 m from the cells. The XRD patterns were obtained in transmission mode; thus, the diffraction pattern is the average of information through the cell thickness at every location. Schematics of the cell components, as well as the geometry of the cell in the X-ray beam are illustrated in the *ESI* (Fig. S1). The cells were mounted on translation stages that raster through the X-ray beam, such that diffraction snapshots were collected across the entire cell with a step size of 1 mm (**Cells 4C-a, 4C-b, 6C-a, 9C-a**) or 0.5 mm (**Cells 6C-b, 6C-c, 9C-b**). The experimental and calibration parameters are provided in the *ESI* (Table S3, S4). Examples of the XRD patterns and the peaks used for analysis in this work are shown in Fig. S2, Section C in the *ESI*. The details on the workflow of data analysis are detailed elsewhere[29].

3 Results and Discussion

Fig. 1 shows the capacity loss for each cell after XFC cycling (450 cycles, shaded color) and the total capacity lost by each cell (solid color). The total loss of each cell includes contributions from the capacity lost during the formation and XFC cycles (*ESI*, *Table S1*). All XRD scans were performed after 450 cycles in the fully discharged condition (3.0 V) after a slow RPT cycle and then storage for 1-2 months. Therefore, any lithium detected on the anode side cannot be reversibly cycled in the cell. Below, we first explore the local and spatially heterogeneous nature of lithium plating and its relationship to the local anode and cathode phases and SOC, followed by calculating the quantitative contribution of irreversible lithium plating and other loss mechanisms to the global cell capacity fade.

3.1 Spatial Correlations between local lithium plating, anode, and cathode SOC

Two-dimensional maps of the spatial distribution of plated lithium over the cell area and the corresponding anode and cathode phases were constructed by rastering the X-ray beam with mm step size over the entire cell area. Spatial maps of the integrated XRD intensity from plated lithium metal and the graphite and lithiated graphite phases are shown in Fig. 2(a-d), while Fig. 2(e-f) shows the corresponding cathode (NMC) unit cell volume and ($\mathbf{0\ 0\ 3}$) peak width (both related to the cathode SOC) for **Cell 6C-b**. Details of the analysis steps are given in the *ESI* (Section C). Regions with plated lithium show a relatively higher intensity of LiC_6 and LiC_{12} (Fig. 2(b, c)), and a relatively lower intensity of graphite (Fig. 2d), compared to areas with little to no plating. Since these maps are obtained in the discharged condition after a slow RPT cycle followed by a 2 h constant voltage hold at 3.0 V and one to two months of storage, all the lithium metal on the anode is 'dead' (i.e. it cannot be stripped or deintercalated from the graphite anode) and the lithium inventory trapped in the graphite can no longer be accessed. In other words, the lithium is electrically disconnected from the anode and thus irreversibly plated. It has been previously hypothesized that this electrically disconnected dead lithium physically blocks the anode lithium underneath it from deintercalation during discharging[20], implying a physical connection between the plated lithium and the anode. Such a physical connection without an electric connection between plated lithium and the graphite anode suggests that a nearly passivating layer is formed between the plated lithium and the anode, due to reaction with the electrolyte. This passivating layer is postulated by Finegan et al. to be a poor conductor of ions and electrons under delithiated conditions which could thus isolate the dead Li.[8]

McShane et al. reported that not all the lithium that plates on the graphite anode during XFC cycling is reversible[16]. Some of this plated lithium is able to strip away during discharging. However, the morphology of the lithium deposits can prevent the plated lithium from completely stripping. This process would create deposits of irreversibly plated Li surrounded by a passivating layer as hypothesized by Fang et al.[10] and Li et al.[30], for lithium plating on a copper substrate. The irreversibly plated Li deposit prevents the deintercalation of lithium from graphite during the slow discharge by increasing the impedance of the most direct path. This results in a further loss of lithium inventory, as hypothesized in Tanim et al.[20] After discharge, as the battery equilibrates, some of the plated Li can, in principle, chemically insert back into the anode. Additionally, the lithium concentration in the anode would equilibrate. However, the poor conductivity of the passivating layer, coupled with the removal of stack pressure from the cells after the 450 XFC cycles ensures that the driving force for both of these reactions is low. Thus, different lithium species (plated lithium and staged graphite) exist during XRD characterization, months after the XFC cycling. The presence of multiple stages of lithiated graphite near the separator underneath irreversibly plated lithium in a discharged state after XFC cycling was also recently reported in Finegan et al. [8] using depth-resolved XRD.

The blocking of lithium in the anode is an additional local degradation mechanism in the battery over XFC cycling. So far, the loss of lithium as dead or trapped lithium, which results in a loss of lithium inventory in the cell, has been discussed. Apart from the LLI, trapped

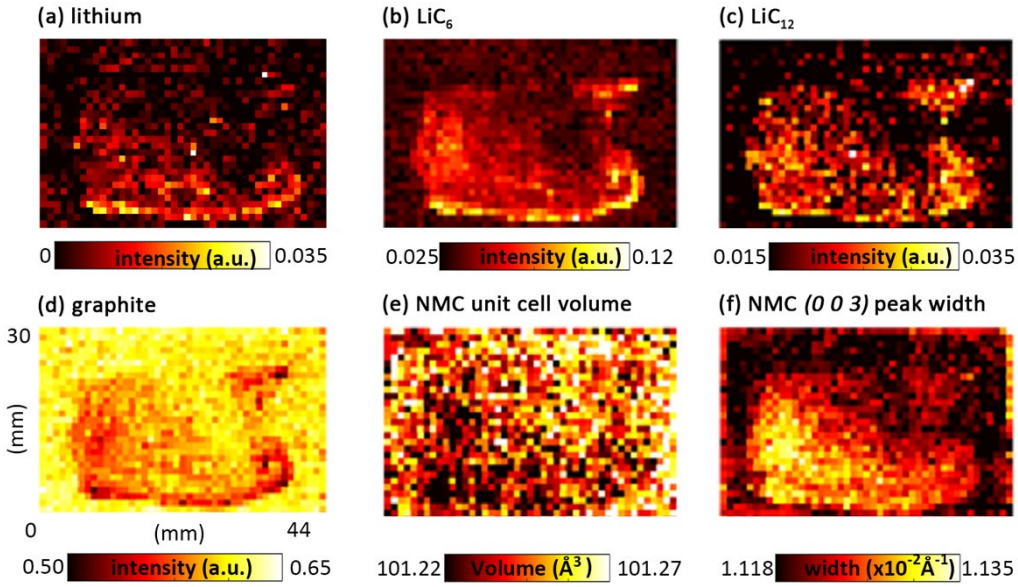

Fig. 2 Spatial maps of irreversibly plated lithium (a) and the anode (b-d) and cathode (e-f) phase, obtained through XRD. On the anode side, the regions with plated lithium directly correlate to regions of higher intensity of LiC_6 in (b) and LiC_{12} in (c) and inversely to graphite intensity (d). As explained in the text, on the cathode, the regions of plated lithium correspond to a lower average cathode SOC (shown by the NMC unit cell volume in (e)) and higher variation in cathode SOC (shown by the width of the NMC ($\mathbf{0\ 0\ 3}$) peak in (f)). The spatial maps are for **cell 6C-b**.

lithium as LiC_6 and LiC_{12} also results in a less active graphite in the anode, since the corresponding volume of graphite anode is unavailable for cycling. To obtain an estimate of the local reduction in active graphite in the anode, three representative regions of **Cell 6C-b** are considered, two of which have little to no lithium plating and one which has a significant amount of lithium plating (see *ESI*, Fig. S4). In the regions with no lithium plating, the ratio of the volume of LiC_6 to graphite shows that **~4%** of the anode is inactive. This reduction in active graphite in regions of no plating is due to formation of LiC_6 during the formation cycles and has been observed recently by McShane et al.[16] In the region with a significant amount of lithium plating, the ratio of graphite and LiC_6 shows that **~25%** of the anode is inactive. Correspondingly, the amount of LiC_6 in the plated region is much larger than in the unplated regions, confirming that this loss of active graphite indeed comes from lithiated graphite trapped under the plated lithium. A few earlier works have discussed a loss of active sites on the anode side, theoretically[6; 31] and experimentally.[6] To our knowledge, no such analysis exists at XFC rates. We note that in the cells used in our study, the anode has a slightly higher capacity than the cathode, in order to minimize lithium plating. Thus, the contribution of this local loss of graphite to the XFC capacity fade of the cells is yet unestablished and examined further in the subsequent sub-sections. *To summarize, locally plated lithium causes lithium to be irreversibly trapped underneath in the anode as LiC_6 and LiC_{12} causing a loss in lithium inventory and, simultaneously, a loss of active material on the anode.*

On the cathode, the regions corresponding to lithium plating show a locally reduced NMC unit cell volume (Fig. 2e). It has been previously demonstrated that the NMC unit cell volume is directly related to the SOC or lithium content[32; 33]. Hence, the regions of the cell with reduced NMC unit cell volume have a lower lithium content (lower SOC). While these unit cell volume variations are modest, the unit cell volume variations in Fig. 2e represent a significant variation in cathode SOC (~2%). This reflects lithium that could not be cycled back into the cathode upon slow discharge. Thus, the loss of lithium locally in the cathode ($Li_xNi_{0.5}Mn_{0.3}Co_{0.2}O_2$) is spatially correlated to lithium lost as irreversibly plated lithium and trapped LiC_6/LiC_{12} in the anode. This SOC variation across the cathode is consistent with lithium following the path of minimum resistance (shortest distance) during discharge, i.e. lithium from unplated regions intercalate into the cathode region just across the separator, rather than into the regions directly opposite to plated regions. In Fig. 2f, we observe that cathode regions directly across regions with lithium plating on the anode also correspond to a larger peak width of the NMC ($\mathbf{0\ 0\ 3}$) peak. The NMC ($\mathbf{0\ 0\ 3}$) peak width is related to the variation in the NMC '*c*' lattice parameter within a single pixel on the image (corresponding to a volume of 0.5 mm x 0.5 mm x cathode thickness of 0.07 mm). The average lithium occupancy for each pixel is given by the peak position, and the spread of lithium concentrations is similarly manisfest as an increase in the peak width (variation in peak positions) . These two spatial maps of the mean and variation in the local cathode SOC reveal an important

finding that the lithium content in the NMC does not fully equilibrate in the discharged state, even after several (1-2) months of rest in the discharged condition. Because the stack pressure applied on the cell during cycling was removed after cycling, it is likely that the cathode particles do not maintain close contact with each other and the current collector, thus not allowing the lithium content in the cathode to spatially equilibrate completely. *Therefore, regions with plated lithium on the anode correspond to a lower average and a higher variation in the cathode SOC*.

We note that the correlations in Fig. 2 are shown for one representative cell (**Cell 6C-b**) charged at **6C** but exist across all cells charged at 6C and above. The *ESI* (Fig. S3) shows similar correlations for **Cells 9C-a, b** charged at **9C**. It is important to note that an in-situ scan allows for a simultaneous local analysis of both electrodes presented thus far, which is harder to accomplish using an ex-situ study (requiring a teardown of the cell and separate analyses of individual cell components). With an ex-situ scan, there is an error associated with the spatial registering of the cathode and anode. In addition, the anode and/or cathode may partly adhere to the separator during cell disassembly, which would result in non-representative results. Thus, an in-situ analysis provides valuable insight into the effect of irreversible lithium plating and other loss mechanisms on both the local and global battery degradation after XFC cycling.

3.2 Quantitative correlation between global XFC capacity fade and total irreversible lithium plating

In order to globally connect the anode phases and their lithium content to the lost cell capacity during XFC, the amount of lithium in metallic lithium and LiC_x is summed over the entire anode. This amount is compared to the amount of NMC over the cell, since NMC serves as an internal reference of known mass. Such an analysis enables us to quantify the individual contributions of distinct lithium loss mechanisms to the global loss of active lithium inventory, which, in turn, can be connected to the XFC capacity loss. In XRD, the mass of any species '*i*' over the entire cell ($\boldsymbol{mass_i}$) can be calculated from the diffraction intensity of that species ($\boldsymbol{I_i^{hkl}}$) corresponding to a diffraction peak with Miller indices ($\boldsymbol{h\,k\,l}$), by using the diffraction intensity ($\boldsymbol{I_{NMC}^{hkl}}$) and volume ($\boldsymbol{V_{NMC}}$) of a known species (NMC in this case) per Equation 1. The ratios of the XRD intensities of various lithium-containing species in the cell with respect to NMC are given in Table 1.

$$\boldsymbol{mass_i} = \left(\frac{\boldsymbol{I_i^{hkl}}}{\boldsymbol{I_{NMC}^{hkl}}}\right)\left(\frac{\boldsymbol{LPF}_{\boldsymbol{NMC}}^{\boldsymbol{hkl}}}{\boldsymbol{LPF}_{\boldsymbol{i}}^{\boldsymbol{hkl}}}\right)\left(\frac{\boldsymbol{m}_{\boldsymbol{NMC}}^{\boldsymbol{hkl}}}{\boldsymbol{m}_{\boldsymbol{i}}^{\boldsymbol{hkl}}}\right)\left(\frac{|\boldsymbol{F}_{\boldsymbol{NMC}}^{\boldsymbol{hkl}}|^2}{|\boldsymbol{F}_{\boldsymbol{i}}^{\boldsymbol{hkl}}|^2}\right)$$
$$\left(\frac{\boldsymbol{cos}\left(\boldsymbol{2\theta}_{\boldsymbol{NMC}}^{\boldsymbol{hkl}}\right)}{\boldsymbol{cos}\left(\boldsymbol{2\theta}_{\boldsymbol{i}}^{\boldsymbol{hkl}}\right)}\right)\left(\frac{\boldsymbol{v_i^2}}{\boldsymbol{v_{NMC}^2}}\right)(\boldsymbol{\rho_i} * \boldsymbol{V_{NMC}}) \qquad (\mathbf{1})$$

In Equation 1, $\boldsymbol{LPF}_{\boldsymbol{i}}^{\boldsymbol{hkl}}$ represents the Lorentz Polarization Factor, $\boldsymbol{m}_{\boldsymbol{i}}^{\boldsymbol{hkl}}$ is the multiplicity, $|\boldsymbol{F}_{\boldsymbol{i}}^{\boldsymbol{hkl}}|$ is the modulus of the structure factor, and $\boldsymbol{\theta}_{\boldsymbol{i}}^{\boldsymbol{hkl}}$ is the Bragg angle, associated with the diffraction peak with Miller indices ($\boldsymbol{h\,k\,l}$) from the species $\boldsymbol{i}$ (*i* = Li, LiC_6, LiC_{12}). $\boldsymbol{v_i}$ is the unit cell volume and $\boldsymbol{\rho_i}$ is the mass density for species $\boldsymbol{i}$. To calculate the diffraction intensities, the ($\mathbf{1\,1\,0}$) peak centered at $\boldsymbol{Q}$ = 2.53 Å^{-1} is used for lithium, the ($\mathbf{0\,0\,3}$) peak centered at $\boldsymbol{Q}$ = 1.32 Å^{-1} is used for NMC, the ($\mathbf{0\,0\,1}$) peak centered at $\boldsymbol{Q}$ = 1.68 Å^{-1} is used for LiC_6 and the ($\mathbf{0\,0\,2}$) peak centered at $\boldsymbol{Q}$ = 1.79 Å^{-1} is used for LiC_{12}. For each species, integrated peak areas from local XRD measurements are summed over the entire cell to obtain the total mass of that species. The detailed steps of the analysis are outlined elsewhere[29]. Thus, using the intensity ratios from *Table 1* in Equation 1, we can calculate the total mass of plated lithium or LiC_x over the entire anode. The loss of lithium inventory during XFC cycling can then be calculated by dividing the total mass of lithium from Li/LiC_x by the initial mass of lithium prior to XFC cycling (calculated from the beginning of life capacity for each cell). We note that the absence of a crystallographic texture in any of the phases is a crucial assumption in Equation 1. As detailed elsewhere,[29] there is no indication of a preferred orientation for the total plated lithium when considering the entire cell.

Fig. 3a shows a quantitative comparison between the full cell XFC capacity loss and loss of inventory inventory from lithium plating, obtained from Equation 1 for all cells. The data points are colored by the charging rate. There is a linear relationship between the LLI from irreversibly plated lithium and cell capacity fade from XFC cycling. A linear fit of the data is shown by the dotted line with a slope of 0.70 ± 0.07 and an R^2 (goodness-of-fit) of 0.83. The fit has a non-zero x-intercept (9.0 ± 1.3 %). This result is consistent with Tanim et al.,[20] where the amount of lithium plating shows a stronger correlation to the loss of cell capacity during XFC cycling, than the C-rate itself. The details for calculating the error bars in Fig. 3a are contained elsewhere[29].

The non-zero x-intercept of the fit (**9.0%**) in Fig. 3a represents a "baseline" capacity fade across all the cells. A large portion of this "baseline" loss is due to the oxidation and reduction reactions occurring at the cathode and anode respectively, resulting in SEI and CEI species. A minor portion of the baseline capacity fade is due to LiC_6 and LiC_{12} trapped in the anode underneath the lithium plated regions, as noted above. There is some lithium inside the anode due the dead lithium blocking the anode from deintcalation, seen as LiC_6 and LiC_{12} intensities (as discussed in Fig. 2). This lithium is also unavailable for cycling and thus a contributor to the LLI in the cells. Fig. 3b shows the contribution of LiC_6 to the LLI as a function of the XFC capacity fade. Unlike with the plated lithium, the total amount of LiC_6 seems largely

independent of the capacity fade or C-rate of the cells. The reason for this is that there is some LiC_6 and LiC_{12} in regions of no lithium plating. This can be seen in Fig. 2(b, c), which shows a non-zero intensity for regions without lithium plating. These LiC_6 and LiC_{12} intensities are independent of lithium plating (XFC cycling) and are likely from the formation cycles. However, since the loss of capacity during formation cycling is different for different cells (see *ESI*, *Table S1*), the amount of LiC_6 in areas without lithium plating is different across the cells. Therefore, the total contribution of LiC_6 to the LLI is relatively independent of the plating (and thus XFC capacity fade) across different cells. Finally, we note that there is also a portion of the baseline capacity which is due to lithium that might not be detected by XRD, at the length scale of this current work. This undetected lithium can be in the form of amorphous Li-containing species, or from metallic lithium where the crystallites do not produce a strong enough XRD peak for the current analysis.

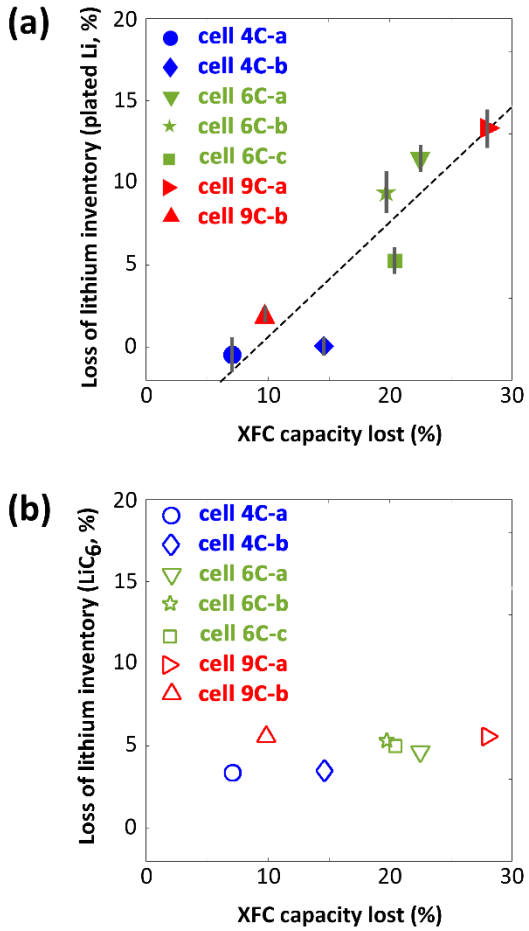

Fig. 3 Relationship between the XFC capacity fade after 450 cycles and the loss of lithium inventory (LLI) due to (a) irreversibly plated lithium and (b) lithium trapped as LiC_6. (a) the cells show a direct correlation between the LLI due to plating and the XFC capacity fade. The goodness of the linear fit shown by the dashed line (R^2) is 0.83, with a slope of 0.70 ± 0.07 and an x-intercept of +9.0%. The amount of lithium lost to LiC_6 (b) is largely independent of the XFC capacity loss.

Next, we quantify the relative amounts of LiC_6 that result from lithium trapped in graphite underneath the plated lithium and those that are independent of the lithium plating. In the regions with no plating, the LiC_6 is either due to the formation cycles or the "baseline" capacity fade during XFC cycles. Thus, in each cell, the amount of LiC_6 in two arbitrarily chosen areas with no lithium plating is calculated. When multiplied by the area of the anode, we calculate the amount of LiC_6 that is independent of lithium plating throughout the cell. Subtracting this amount from the total amount of LiC_6 furnishes the amount of LiC_6 that is trapped as a direct result of the plated lithium, during XFC cycling. The detailed calculations for LiC_6 are provided in the *ESI* (Table S5). The LLI from LiC_6 during XFC cycling is **~0-2.1%** of the XFC capacity fade, and contributes much less to the loss of lithium inventory compared to plated lithium in the cells with a significant amount of lithium plating (**cell 6C-a**, **6C-b**, **6C-c**, **9C-a**). A similar calculation shows that the contribution of trapped lithium in the LiC_{12} to the LLI is also very small at **~0-0.3%**.

Cell	$\frac{I_{Li}}{I_{NMc}}$	$\frac{I_{LiC_6}}{I_{NMc}}$	$\frac{I_{LiC_{12}}}{I_{NMc}}$	NMC unit cell volume
	(x 10^{-4})	(x 10^{-3})	(x 10^{-3})	(Å^3)
4C-a	-	6.4	0.7	101.48
4C-b	0.07	6.5	1.3	101.34
6C-a	6.91	8.7	1.2	101.17
6C-b	5.75	10.0	3.4	101.24
6C-c	3.26	9.5	2.4	101. 25
9C-a	8.27	10.7	3.2	101. 10
9C-b	1.15	10.6	1.2	101. 42

Table 1 Intensity ratios of Li, LiC_6 and LiC_{12} with respect to NMC, as used in Equation 1 to obtain Fig. 3. The last column is the NMC unit cell volume, used to calculate the lithium occupancy in NMC shown in Fig. 4.

Thus, after accounting for the LLI due to plated lithium and lithium trapped as LiC_6 and LiC_{12}, the rest of the baseline capacity fade across cells comes from electrolyte reduction/oxidation and possible reaction of lithium with the respective species to form SEI/CEI products including organic polycarbonates and inorganic halides and oxides like LiF and Li_2O [34] or CEI (cathode-electrolyte interphase) products[35]. Such reactions also result in a loss in lithium inventory of the cell. Since these reaction products are amorphous or nanocrystalline, they are not detectable by XRD. We note that **Cell 4C-a** showed little lithium plating and an XFC capacity fade of **~7%**. Two nominally identical cells to **Cell 4C-a** were

cycled similarly in a complementary study at the same C-rate and charge protocol as **Cell 4C-a** also showed a **7-8%** capacity fade over 450 XFC cycles, with little lithium plating, indicating a capacity fade stemming primarily from side reactions (SEI/CEI).[20] *Thus, depending on the capacity lost in the cell, either irreversible lithium plating or formation of SEI/CEI is the major contributor to the loss of lithium inventory, while the remnant lithium in the anode as lithiated graphite is a minor contributor.*

Fig. 3 captures the link between the cell capacity fade and the loss of lithium in Li-containing species measured by XRD after 450 XFC cycles. Looking deeper into Fig. 3(a), there are certain intriguing, anecdotal observations. For example, **Cell 9C-b** has a lower capacity fade but a higher amount of lithium plating-related losses compared to **Cell 4C-b**. The large difference in C-rates (9C vs 4C) and charging protocols (two-step vs five-step constant current protocol, see *Table S1*, *ESI*) between these two cells is likely to play a factor in this difference. At lower C-rates, **Cell 4C-b** spends more time at higher voltages. Additionally, these cells have a higher charge acceptance for the same voltage range in Fig. 1 in Tanim et al. [20] These factors are likely to accelerate electrolyte decomposition and SEI/CEI formation[36] compared to **Cell 9C-b**, which is cycled at a higher C-rate and has a relatively lower charge acceptance.

3.3 Quantitative link between total capacity loss of the cell, loss of lithium inventory and loss of active material

So far, various LLI mechanisms have been quantified. Additionally, there is a loss of active graphite (as discussed in Section 3.1). In order to quantify the contribution of all LLI mechanisms to the overall capacity fade, we expand the local analysis in Fig. 2e to cover the entire cathode to obtain a quantitative relationship between total LLI and the total capacity loss of the cells. An earlier operando study showed that the average volume of the NMC unit cell is directly correlated with the lithium concentration (or SOC) in the cathode[32]. To use this methodology to determine cathode SOC, a reference NMC unit cell volume is needed. We obtained XRD data for a pristine cell prior to formation cycling. This pristine cell unit cell volume of NMC corresponds to the initial lithium inventory (1.02 lithium atoms per unit cell of NMC) prior to any cycling (see *ESI*, Table S6). Subsequently, the average change in NMC unit cell volume is calculated for each cell after XFC cycling relative to the pristine cell. The average lithium occupancy per NMC unit cell is then calculated from the change in NMC unit cell volume, using Table 1 and Table S1 from[32]. The difference in Li occupancy in the pristine cell compared to the cells after XFC cycling is due to the irreversible loss of lithium over cycling. This lithium occupancy is then compared to the total capacity in each cell (Fig. 4). A linear fit to these data yields a slope of 0.98 ± 0.02 and a y-intercept of 2.50 ± 1.78% (R-square: 0.99). The linear correlation with near-zero intercept shows that the average NMC unit cell volume (lithium inventory) is an excellent tracker of the cell capacity.

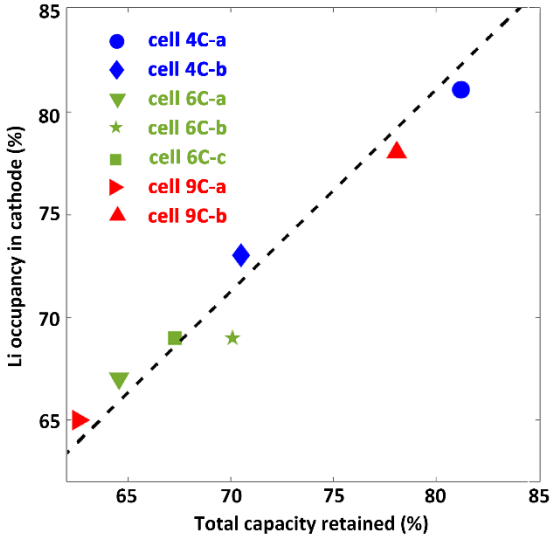

Fig. 4 Correlation between the lithium occupancy per unit cell in NMC (compared to a pristine, uncycled cell) and the total capacity retained by the cells over formation and XFC cycling. The dotted lie indicates a linear fit of the data, with a slope of 0.98 ± 0.02 (R^2: 0.99).

Previous works have highlighted the role of the loss of active material due to physical deterioration of the cathode and anode [6; 37] due to cracking leading to particle separation in determining capacity fade in the cells, differentiating LLI and LAM dominated loss as *'inventory limited'* and *'site limited'* cells respectively.[12] In an earlier work with similar cells using thinner electrodes, the physical degradation of the cathode was seen to play the dominant role in the cell performance.[28] A comparison with the earlier study highlights the role of electrode thickness in determining the primary mode of degradation in the cells during XFC cycling.[38] A decrease in electrode thickness resulted in *site limited* performance, with cell degradation dominated by LAM and not LLI from Li plating in Tanim et al.[28] The current work with thicker electrodes shows the cells are primarily *inventory limited*, since the overall cell capacity loss is completely captured by the total LLI. This transition in the primary degradation mode is due to increased lithiation gradients and heterogeneous current densities[8] in the thicker electrodes that accelerate the LLI compared to thinner electrodes. Hence, in this study, *the loss of lithium inventory is the primary driver of deterioration of cell capacity at XFC rates, while the effect of loss of active material on cell capacity is negligible.*

4 Conclusions

Spatially resolved high-energy X-ray diffraction was employed to non-destructively quantify the local and global loss mechanisms in extreme fast charging of lithium-ion batteries. Locally, irreversible lithium plating on the anode is observed to be spatially heterogeneous and the regions with plated lithium on the anode are co-located with regions of trapped LiC_6 and LiC_{12} within the anode, which further depletes the active lithium inventory in the cell. These regions also correspond to a locally reduced SOC in the NMC cathode in the discharged state, consistent with the loss of lithium on the anode side. Globally, the total amount of irreversibly plated lithium on the anode is directly correlated to the capacity fade of the cell across the C-rates studied and is the primary driver of capacity fade during XFC cycling. Additionally, LLI from trapped LiC_6 and LiC_{12} in the anode due to lithium plating is a minor contributor to XFC capacity fade. SEI related losses appear independent of lithium plating. Thus, the analysis on the anode side enables the separation of individual LLI mechanisms and the quantification of their relative contributions to the battery performance. On the cathode side, the overall capacity fade of the battery is directly correlated to the LLI in the fully discharged state. This result shows that the cells are *inventory limited* with LLI playing a primary role in the deterioration of cell performance rather than the LAM on either electrode. Therefore, the cathode side analysis can be leveraged to keep track of the overall dominant mechanism of cell degradation, irrespective of the individual loss mechanisms within LLI.

It is imperative to quantify the contributions of different capacity fading mechanisms in order to unravel the factors that affect batteries' cyclability, yet the complexity of real cells makes such a quantification approach challenging. In this paper, we have adopted a methodology that uses in-situ XRD to obtain a 2D map of the entire cell, enabling us to quantify the capacity loss originating from SEI growth, lithium plating, and lithium trapped in staged graphite, as well as the loss of active material. Such a simultaneous analysis of different battery components, enabled by an in-situ data acquisition, provides a pathway towards developing a comprehensive understanding of lithium plating and its effect on local and global battery degradation under extreme fast charging conditions. This understanding will in turn inform strategies for designing the next generation of lithium-ion batteries, enabling a consistent and safe performance over XFC cycling. Some strategies for preventing nucleation of parasitic lithium plating that contribute to the XFC capacity fade include tailoring the anode microstructure to enhance electrolyte wetting in the anode and optimizing the charging protocol, and the cycling pressure[14].

Author Contributions

PPP, VT and CC conducted the XRD-based experiments. PPP, VT, CC, H-GS, MFT and JNW participated in the XRD analysis and interpretation of data, as well as writing the manuscript. ANJ, SET, and ARD designed, assembled, and formed the pouch cells. TRT and EJD did the XFC cycling and electrochemical analyses of the cells and discussed the XRD data interpretation. MFT, JNW and EJD were responsible for funding acquisition.

Conflicts of interest

There are no conflicts to declare.

Acknowledgements

Funding was provided from the Vehicle Technologies Office of the U.S. Department of Energy's Office of Energy Efficiency and Renewable Energy under the guidance of the Advanced Battery Cell Research Program (eXtreme fast charge Cell Evaluation of Lithium-ion batteries, XCEL). The manuscript has been authored by SLAC Linear Accelerator Laboratory, operated by Stanford University under Contract No. DE-AC02-76SF00515. Cell assembly was done at the CAMP facility at Argonne National Laboratory, which is a U.S. Department of Energy Office of Science Laboratory operated by UChicago Argonne, LLC under Contract No. DE-AC02-06CH11357. Testing and cycling of the cells were carried out under the Battelle Energy Alliance, LLC under Contract No. DE-AC07-05ID14517 for Idaho National Laboratory with the U.S. Department of Energy. The XRD experiments were conducted at the beamline 11-ID-B at the Advanced Photon Source, operated by Argonne National Laboratory and at beamline 28-ID-2 at National Synchrotron Light Source II, operated by Brookhaven National Laboratory under Contract No. DE-SC0012704. Drs. Olaf Borkiewicz, Uta Ruett and Jiaming Bai helped set up the XRD experiments at APS and NSLS-II. Part of the post-processing was carried out using computational resources from Extreme Science and Engineering Discovery Environment (XSEDE), funded by the National Science Foundation under contract ACI-1053575.

References

1 NEUBAUER, J.; WOOD, E. The impact of range anxiety and home, workplace, and public charging infrastructure on simulated battery electric vehicle lifetime utility. **Journal of Power Sources,** v. 257, p. 12-20, 2014.

2 SHABBIR, A. et al. Enabling fast charging — a battery technology gap assessment. **Journal of Power Sources,** v. 367, p. 250-262, 2017.

3 TANIM, T. R. et al. Electrochemical Quantification of Lithium Plating: Challenges and Considerations. **J. Electrochem Soc.,** v. 166, n. 12, p. A2689-A2696, 2019.

4 MUSSA, A. S. et al. Fast-charging to a partial state of charge in lithium-ion batteries: A comparative ageing study. **Journal of energy Storage,** v. 13, p. 325-333, 2017.

5 WALDMANN, T.; HOGG, B. I.; WOHLFAHRT-MEHRENS, M. Li plating as unwanted side reaction in commercial Li-ion cells–A review. **Journal of Power Sources,** v. 384, p. 107-124, 2018.

6 BIRKL, C. R. et al. Degradation diagnostics for lithium ion cells. **Journal of Power Sources,** v. 341, p. 373-386, 2017.

7 LIU, Y.; ZHU, Y.; CUI, Y. Challenges and opportunities towards fast-charging battery materials **Nature Energy,** v. 4, p. 540-550, 2019.

8 FINEGAN, D. et al. Spatial dynamics of lithiation and lithium plating during high-rate operation of graphite electrodes. **Energy and environmental Science**, 2020.

9 COLCLASURE, A. et al. Electrode scale and electrolyte transport effects on extreme fast charging of lithium-ion cells. **Electrochemica Acta,** v. 337, p. 135854, 2020.

10 FANG, C. et al. Quantifying inactive lithium in lithium metal batteries. **Nature,** v. 572, p. 511-515, 2019.

11 LI, W. et al. Formation and Inhibition of Metallic Lithium Microstructures in Lithium Batteries Driven by Chemical Crossover. **ACS Nano,** v. 11, n. 6, p. 5853-5863, 2017.

12 TORNHEIM, A.; O'HANLON, D. What do Coulombic Efficiency and Capacity Retention Truly Measure? A Deep Dive into Cyclable Lithium Inventory, Limitation Type, and Redox Side Reactions. **Journal of The Electrochemical Society**, p. 110520, 2020.

13 CHEN, B.-R. et al. A machine learning framework for early detection of lithium plating combining multiple physics-based electrochemical signatures. **Cell Reports Physical Science**, p. 100352, 2021. ISSN 2666-3864.

14 PAUL, P. P. et al. A Review of Existing and Emerging Methods for Lithium Detection and Characterization in Li-Ion and Li-Metal Batteries. **Advanced Energy Materials,** v. n/a, n. n/a, p. 2100372, 2021. ISSN 1614-6832. Disponível em: < https://onlinelibrary.wiley.com/doi/abs/10.1002/aenm.202100372 >.

15 SOMERVILLE, L. et al. The effect of charging rate on the graphite electrode of commercial lithium-ion cells: A post-mortem study. **Jpurnal of Power Sources,** v. 335, p. 189-196, 2016.

16 MCSHANE, E. et al. Quantification of Inactive Lithium and Solid Electrolyte Interphase (SEI) Species on. **ACS Applied Energy Letters,** v. 5, n. 6, p. 2045–2051, 2020.

17 BURNA, J. C.; STEVENES, D. A.; DAHN, J. R. In-Situ Detection of Lithium Plating Using High Precision Coulometry. **Journal of the Electrochemical Society,** v. 162, n. 6, p. A959-A964, 2015.

18 GOLD, L. et al. Probing lithium-ion batteries' state-of-charge using ultrasonic transmission – Concept and laboratory testing. **Journal of Power Sources,** v. 343, p. 536-544, 2017.

19 BOMMIER, C. et al. In Operando Acoustic Detection of Lithium Metal Plating in Commercial LiCoO2/Graphite Pouch Cells. **Cell Reports Physical Science**, p. 100035, 2020.

20 TANIM, T. et al. Heterogeneous Behavior of Lithium Plating during Fast Charging. **Cell Reports Physical Science**, p. 100114, 2020.

21 STEINRÜCK, H.-G. et al. Toward quantifying capacity losses due to solid electrolyte interphase evolution in silicon thin film batteries. **The Journal of Chemical Physics**, p. 084702, 2020.

[22] TOMASZEWSKA, A. et al. Lithium-ion battery fast charging: A review. **eTransportation,** v. 1, n. 100011, 2019.

[23] GALLAGHER, K. et al. Optimizing Areal Capacities through Understanding the Limitations of Lithium-Ion Electrodes. **Journal of The Electrochemical Society,** v. 163, n. 2, p. A138-A149, 2016.

[24] GAO, T. et al. Interplay of Lithium Intercalation and Plating on a Single Graphite Particle. **Joule**, 2021. ISSN 2542-4351.

[25] SHI, F. et al. Strong texturing of lithium metal in batteries. **PNAS,** v. 114, n. 46, p. 12138-12143, 2017.

[26] YULAEV, A. et al. From Microparticles to Nanowires and Back: Radical Transformations in Plated Li Metal Morphology Revealed via in Situ Scanning Electron Microscopy. **Nanloletters,** v. 18, n. 3, p. 1644-1650, 2018.

[27] YAO, K. et al. Quantifying lithium concentration gradients in the graphite electrode of Li-ion cells using operando energy dispersive X-ray diffraction. **Energy & Environmental Science**, 2019.

[28] TANIM, T. R. et al. Extreme Fast Charge Challenges for Lithium-Ion Battery: Variability and Positive Electrode Issues. **J. Electrochem Soc.,** v. 166, n. 10, 2019.

[29] PAUL, P. et al. Using in-situ X-ray Diffraction to Examine Behavior and Degradation of Lithium Ion Batteries from Extreme Fast Charging. **In Preparation**, 2021.

[30] LI, Y. et al. Correlating structure and function of battery interphases at atomic resolution using cryoelectron microscopy. **Joule,** v. 2, n. 10, p. 2167-2177, 2018. ISSN 2542-4351.

[31] SANTHANAGOPALAN, S. et al. Parameter Estimation and Life Modeling of Lithium-Ion Cells. **Journal of The Electrochemical Society,** v. 155, n. 4, p. A345-A353, 2008.

[32] DEBIASI, L. et al. Between Scylla and Charybdis: Balancing Among Structural Stability and Energy Density of Layered NCM Cathode Materials for Advanced Lithium-Ion Batteries. **Journal of Physical Chemistry C,** v. 121, p. 26163−26171, 2017.

[33] DOLOTKO, O. et al. Understanding structural changes in NMC Li-ion cells by in situ neutron diffraction. **Journal of Power Sources,** v. 255, p. 197-203, 2014.

[34] VERMA, P.; MAIRE, P.; NOVÁK, P. A review of the features and analyses of the solid electrolyte interphase in Li-ion batteries. **Electrochemica Acta,** v. 55, n. 22, p. 6332-6341, 2010.

[35] FANG, S. et al. Anode-originated SEI migration contributes to formation of cathode-electrolyte interphase layer. **Journal of Power Sources,** v. 373, p. 184-192, 2018.

[36] SMITH, A. et al. A high precision coulometry study of the SEI growth in Li/graphite cells. **Journal of The Electrochemical Society,** v. 158, n. 5, p. A447, 2011.

[37] YAN, P. et al. Intragranular cracking as a critical barrier for high-voltage usage of layer-structured cathode for lithium-ion batteries. **Nature Communications,** v. 8, n. 14101, 2017.

[38] CHINNAM, P.; CHEN, B.-R.; TANIM, T. Aging dynamics during fast charge: cell design versus material degradation. **In preparation**, 2021.